AIAA JOURNAL
Vol. 48, No. 11, November 2010

Induced-Drag Minimization of Nonplanar Geometries Based on the Euler Equations

Jason E. Hicken* and David W. Zingg†
University of Toronto, Toronto, Ontario M3H 5T6, Canada

DOI: 10.2514/1.J050379

The induced drag of several nonplanar configurations is minimized using an aerodynamic shape optimization algorithm based on the Euler equations. The algorithm is first validated using twist optimization to recover an elliptical lift distribution. Planform optimization reveals that an elliptical planform is not optimal when side-edge separation is present. Optimized winglet and box-wing geometries are found to have span efficiencies that agree well with lifting-line analysis, provided the bound constraints on the entire geometry are accounted for in the linear analyses. For the same spanwise and vertical bound constraints, a nonplanar split-tip geometry outperforms both the winglet and box-wing geometries, because it can more easily maximize the vertical extent at the tip. The performance of all the optimized geometries is verified using refined grids consisting of 88–152 million nodes.

Nomenclature

b	=	wing span
C_D	=	coefficient of drag
$C_{D,\text{ellip}}$	=	C_D for an elliptical lift distribution
C_L	=	coefficient of lift
c	=	sectional chord length
c_d	=	sectional drag length
c_l	=	sectional lift coefficient
D	=	drag
e	=	span efficiency
L	=	lift
M	=	Mach number
q_∞	=	freestream dynamic pressure
S	=	reference area
U_∞	=	freestream velocity magnitude
α	=	angle of attack with respect to the root chord
Γ	=	circulation distribution
Λ	=	aspect ratio
ρ_∞	=	freestream density

I. Introduction

FUEL-SUPPLY uncertainty and climate-change mitigation demand action from all transportation sectors. Addressing these challenges will likely require multiple strategies, including efficiency improvements. To this end, drag reduction remains a critical area of research for the aviation industry.

Induced drag, also called vortex drag, is an inviscid form of drag experienced by lifting wings of finite span. It is the result of work done on the fluid to sustain the kinetic energy in the trailing vortical wake. Induced drag represents approximately 40% of the total drag on a conventional aircraft in cruise flight [1], so concepts that reduce vortex drag are certainly worth studying. This is the motivation behind the present study of nonplanar configurations and their optimal design.

Roughly speaking, nonplanar configurations are geometries that produce wakes with vertical structure. Munk [2] established a number of fundamental results concerning such nonplanar configurations. Among his contributions, Munk showed that nonplanar configurations can have significantly lower induced drag relative to planar wings with the same span and lift. The example given by Munk is an optimally loaded circular ring-wing, which has half the induced drag of an optimally loaded planar wing. In the decades following Munk's work, nonplanarity has been the subject of numerous studies. We mention a few notable examples here, primarily analytical and numerical results. For a more complete review see [1].

Induced-drag theory for nonplanar configurations was extended by Cone [3] to include general circulation distributions. Cone also considered the induced drag on a number of optimally loaded configurations. In particular, he showed that the elliptical distribution is optimal for families of closed elliptical loops, including the line and circle as limiting cases.

Mangler's [4] analysis of end-plate configurations presaged later work on winglets. His results were refined and generalized by Lundry and Lissaman [5], who presented a method to accurately evaluate the induced drag of nonplanar configurations consisting of line segments. The induced drag analysis of wing-tip geometries was further generalized by Lowson [6]. He represented winglets as polynomial curves and superelliptic functions. While the vertical end-plate is optimal, Lowson found that superelliptical functions of modest degree can achieve near-optimal induced drags.

Van Dam [7] studied planar geometries that produce nonplanar wakes at angle of attack. While his initial results were shown to be overly optimistic due to numerical errors [8], the idea of exploiting planform shape has merit. This is supported by Smith's work with a planar split-tip configuration [9], which was shown to reduce the induced drag by 6% according to linear theory. More impressive still, a nonlinear analysis using wake relaxation showed a 10% reduction relative to an optimally loaded planar wing.

Smith's work with the split-tip configuration illustrates a serious drawback with linear theory: the static-wake assumption. This assumption is adequate for a first-order analysis of most geometries, but the split-tip example demonstrates that higher-order effects must be included for accurate induced drag prediction.

Wake shape is one way that nonlinearity can impact the induced drag. Another important higher-order effect is induced lift, which, unlike wake shape, is unique to nonplanar configurations. Induced lift is generated on nonplanar geometries by the vertical component of the bound vortex, which increases or decreases the streamwise velocity on parts of the geometry. For fixed lift, Cone [3] argued that induced

Presented as Paper 2008-5807 at the 12th AIAA/ISSMO Multidisciplinary Analysis and Optimization Conference, Victoria, British Columbia, Canada, 10–12 September 2008; received 4 December 2009; revision received 11 June 2010; accepted for publication 15 June 2010. Copyright © 2010 by Jason E. Hicken and David W. Zingg. Published by the American Institute of Aeronautics and Astronautics, Inc., with permission. Copies of this paper may be made for personal or internal use, on condition that the copier pay the $10.00 per-copy fee to the Copyright Clearance Center, Inc., 222 Rosewood Drive, Danvers, MA 01923; include the code 0001-1452/10 and $10.00 in correspondence with the CCC.

*Postdoctoral Fellow, Institute for Aerospace Studies. Member AIAA.
†Professor and Director, Institute for Aerospace Studies, Canada Research Chair in Computational Aerodynamics, J. Armand Bombardier Foundation Chair in Aerospace Flight. Associate Fellow AIAA.

lift leads to lower induced drag on configurations with positive spanwise camber (e.g., winglets oriented upward) and higher induced drag on configurations with negative spanwise camber (e.g., winglets oriented downward). This was confirmed by Eppler using lifting-surface theory with induced lift contributions [10].

One of the aims of this paper is to study the impact of nonlinear effects on induced drag by employing an Euler-based optimization. While computational fluid dynamics (CFD) introduces its own set of issues to induced drag prediction, there are several advantages to using CFD in this context. Most obviously, induced lift contributions and nonlinear wake-wing interactions are inherently included in the analyses. Moreover, the Euler equations model the wake automatically and do not require the user to prescribe where the wake begins, although the separation location on wing tips may not match the true viscous flow (see discussion in Sec. II.B). Finally, the Euler equations can be used to accurately model wave drag, and they can be extended naturally to the Navier–Stokes equations.

While CFD analyses of induced drag are becoming more common, the use of aerodynamic shape optimization (ASO) to minimize exclusively induced drag is much less common. The focus within the ASO literature has been the minimization of wave drag and, to a lesser extent, viscous drag. When induced drag is considered, a low-fidelity model is often used to find an optimal geometry, which is subsequently analyzed using an Euler flow solver (see, for example, [11,12]). A clear drawback with this approach is that the geometry has not be optimized with respect to the Euler equations.

Two notable investigations of induced drag in the ASO literature are the works of Yamazaki et al. [13] and Liersch et al. [14]. Yamazaki et al. [13] used drag decomposition and a genetic algorithm to explore the tradeoffs between minimizing different components of drag, including induced drag. Liersch et al. [14] were interested in whether or not nonplanar wings outperform planar wings when both have the same unfolded span (i.e., equal spanwise arclength). They used a lifting-line method to probe the design space initially, while Euler-based inverse design and drag minimization were used to refine the twist in some cases. Their study produced a number of interesting results. In particular, they concluded that there exist nonplanar wings with lower induced drag than a planar wing with the same unfolded span and elliptical planform.

In this work, our primary objective is explore the use of Euler-based aerodynamic shape optimization to minimize induced drag. The algorithm and methodology are described in Sec. II. As a validation, we use twist optimization to recover an elliptical lift distribution (Sec. III). We believe this to be an important, yet often overlooked, benchmark for high-fidelity ASO algorithms. In the same section, we demonstrate the subtleties of planform optimization. Subsequently, we investigate several nonplanar geometries: the winglet-up and winglet-down configurations in Sec. IV, the box-wing configuration in Sec. V, and the split-tip configuration in Sec. VI. These studies also accomplish our secondary objectives, namely, demonstrating the capabilities of the Newton–Krylov ASO algorithm and illustrating the potential of exploratory ASO to reveal novel design concepts. Our results are summarized in Sec. VII, where we also provide some discussion and conclusions.

II. Methodology

A. Aerodynamic Shape Optimization Algorithm

This section contains a brief summary of the ASO algorithm to familiarize the reader with our approach. The algorithm is thoroughly described and verified in [15].

We use B-spline volumes to integrate geometry parameterization with mesh movement. Each block in the computational mesh is represented using a B-spline tensor-product volume. B-spline surfaces are extracted from the volumes bordering the aerodynamic surface, and the control-point coordinates of these surfaces become the geometric design variables. See Fig. 1 for an example illustrating the geometry parameterization. The surface control points are coupled to the volume control points using the equations of linear elasticity. Specifically, a linear elasticity mesh-movement algorithm is applied to the mesh of B-spline control points, rather than the individual points of the flow-analysis mesh. Once the control-point locations have been determined, the flow-analysis mesh is regenerated algebraically using the B-spline equation. This semi-algebraic approach produces perturbed grids in 2–3 orders of magnitude less time relative to a node-based linear elasticity method, and yields grids of similar quality [15]. Moreover, the integrated parameterization and mesh-movement algorithm can accommodate large shape changes, which is critical in the context of exploratory shape optimization.

Our flow solver uses second-order accurate summation-by-parts (SBP) finite difference operators to discretize the Euler equations [16,17]. Simultaneous approximation terms (SATs) are applied at block boundaries to enforce boundary conditions and couple blocks [18]. The SAT interface treatment is similar to the interelement coupling that arises in the discontinuous Galerkin finite element method [19,20]. The SBP–SAT discretization is linearly time-stable and requires only C^0 mesh-line continuity. Fourth-difference scalar dissipation is introduced to prevent oscillations. We avoid using second-difference numerical dissipation, since it can significantly degrade the accuracy of the induced drag prediction.

We use a parallel Newton–Krylov algorithm to solve the discrete equations. The Krylov solver is preconditioned using an approximate-Schur preconditioner [21], and Newton's method is globalized using a dissipation-based continuation method [22]. The solver is considered converged when the l_2 norm of the residual has been reduced 10 orders of magnitude. Further details regarding the flow solver are available in [23].

The SNOPT algorithm [24] is used to find locally optimal designs. The algorithm uses a sequential quadratic programming method and can handle nonlinear constraints. The Hessian of the Lagrangian is approximated using the quasi-Newton method of Broyden, Fletcher, Goldfarb, and Shanno (BFGS); the full-memory version of BFGS is used here. The optimizations are considered converged when the Karush–Kuhn–Tucker conditions are satisfied to within a tolerance of $\varepsilon = 10^{-7}$.

SNOPT requires the gradient of the objective and the constraints. We use the discrete-adjoint variables to calculate the gradient of functionals that depend on the flow. The adjoint equation corresponding to the flow residual is solved using flexible GCROT(m, k)

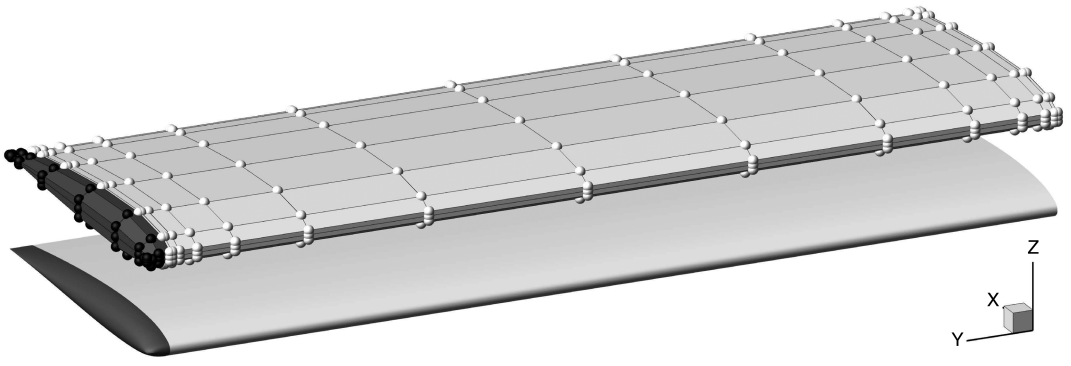

Fig. 1 Example B-spline control mesh (upper) and surface (lower) used for the twist and planform optimization cases; the wing tip is parameterized using the black control points and is constrained by the movement of the inner control points, shown as white spheres.

with the approximate-Schur preconditioner; GCROT(m, k) has been shown to be robust and efficient compared with several other truncated Krylov-subspace methods [25].

Gradient-based optimization algorithms, like SNOPT, perform a local search of the design space, and there is no guarantee that they will find the global optimum. The studies presented below use a modest number of degrees of freedom, and experience suggests that the design space is not particularly complex; hence, a multistart strategy is often effective in locating additional local optima. More complicated optimization problems will require an automated and efficient search of the design space, and this remains an active area of research.

B. Induced Drag Prediction

Induced drag is notoriously difficult to evaluate accurately. This difficulty is observed in panel codes as well as Euler and Navier–Stokes solvers. It has been attributed to the thin shape of wings, poorly resolved pressure gradients, and fore-aft subtractive cancellation [8].

Modern panel codes model the wake roll-up explicitly by solving for the shape of the wake. Smith and Kroo [8,26] developed a hybrid method to determine the wake shape and used this method to study elliptical and crescent-shaped planforms. Their study showed that modelling the wake shape is important for nonplanar configurations, even when the nonplanar wake is a consequence of trailing-edge shape as it is for the elliptical planform. They also concluded that a Trefftz-plane integration is more reliable than surface-based integration for induced drag prediction, but only if the wake shape is accurately modeled.

Induced drag can also be predicted from numerical solutions of the Euler equations; however, as mentioned in the introduction, this approach is not without difficulties. Van Dam and Nikfetrat [27] and van Dam et al. [28] were among the first to address the issues associated with calculating induced drag in Euler flow solvers. Similar to panel codes, surface-based integration was found to be less accurate than wake-plane-based integration techniques. Wake-plane analysis also provides the means to decompose the drag into different components (induced drag, viscous drag, etc.). The vorticity in the wake can decay before reaching the wake-analysis plane due to the numerical dissipation in CFD solvers. More recent wake-plane analyses account for this transfer of energy by including entropy contributions in the induced drag calculation [29–31].

We have experimented with the wake-plane analysis of Giles and Cummings [32] in an attempt to address the difficulties associated with accurate prediction of induced drag. In our experience, the wake-plane drag prediction is more accurate on coarse grids, but of similar accuracy to surface-based integration on finer grids. In addition, we have observed nonmonotonic convergence of wake-based induced drag on fine grids.

Based on our mixed experience with wake-based drag analysis, we have elected to use sufficiently fine mesh spacing to offset the potential problems of surface-based drag prediction. Table 1 lists the statistics for the baseline grids used in the following studies. Some variation in the mesh spacing will occur when the grids are perturbed. However, the wall-normal spacing remains on the order of 10^{-3} for the duration of an optimization. To confirm the predicted forces on the optimal designs, we repeat the flow analysis for these shapes using refined grids with a factor of 3 to 4 more nodes in each coordinate direction. The refined grids are obtained using the B-spline volumes, which ensures that the surface nodes coincide with the predicted optimal shapes. Table 1 lists representative statistics for the refined grids immediately below their corresponding coarse grids. The refined grids are used to produce all spanwise lift- and drag-distribution plots.

Table 1 Dimensions and length parameters (in root-chord units) for the grids used in the studies

Study	Blocks	Grid size	Spacing		Far-field distance[b]
		(Nodes)	Off-wall	Surface[a]	
Twist, planform					
Coarse	18	1 381 050	0.00374	0.0278	36.8
Fine	1152	88 387 200	0.00086	0.0070	36.8
Winglet, box wing					
Coarse	48	5 647 152	0.00072	0.0153	22.0
Fine	1296	152 473 104	0.00013	0.0060	22.0
Wing with split tip					
Coarse	42	3 827 250	0.00050	0.0187	22.0
Fine	1134	103 335 750	0.00017	0.0062	22.0

[a]Average surface spacing $\equiv \sqrt{S/N_{\text{surf}}}$, where S is the area, and N_{surf} is the number of cells on the surface.
[b]Minimum distance to the far-field boundary.

The far-field boundary is at least 22 chord lengths from the surface geometry on all grids. In their study, Phillips et al. [12] found that doubling the far-field distance from 10 to 20 chord lengths changed the induced drag by less than 1%, which suggests that 22 chord lengths is a conservative choice.

Euler codes often produce tip vortices that release off the side of the wing tip, rather than at the trailing edge. This side-edge separation deserves some discussion, because it influences the induced drag by creating a nonplanar wake (see [9] as well as Sec. III). While its accurate prediction with an Euler code is debatable, edge separation is a real phenomenon [33], which has even been observed on wings with rounded tips [34,35]. Thus, the perspective taken here is to study the role of edge separation on induced drag, while acknowledging that the separation location and vortex size may not correspond with the true (viscous) flow.

C. Definitions and Conventions

We use the freestream values of the density and sound speed to nondimensionalize the flow variables. The characteristic length is the initial root chord of the configuration. For all of the studies we use a fixed Mach number of $M = 0.5$. This Mach number ensures that the flow remains subsonic for the geometries considered. We acknowledge that practical aerodynamic designs must consider multiple operating conditions; however, induced drag depends only weakly on Mach number [9], so our conclusions should be applicable to a wide range of flows.

The coefficients of lift and drag are defined as

$$C_L = \frac{L}{q_\infty S} \quad \text{and} \quad C_D = \frac{D}{q_\infty S}$$

respectively, where S is the reference area (see subsequent discussion) and $q_\infty = \frac{1}{2}\rho_\infty U_\infty^2$ is the dynamic pressure. When only vortex drag is present, the coefficient of drag can be expressed as

$$C_D = \frac{C_L^2}{\pi \Lambda e} = \frac{C_{D,\text{ellip}}}{e} \tag{1}$$

where $\Lambda = b^2/S$ is the aspect ratio, b is the span, and $C_{D,\text{ellip}}$ is the minimum induced drag predicted by lifting-line theory for a planar wake. The parameter e is the span efficiency. Ideally, the span efficiency would depend only on geometry, but, in general, it may be a function of the coefficient of lift [1]. However, this dependence is often weak, so span efficiency remains a useful and popular means of comparing the induced drag of different configurations.

Rearranging Eq. (1) we have

$$e = \frac{C_L^2}{\pi \Lambda C_D} = \frac{L^2}{q_\infty b^2 D}$$

This suggests there are two distinct ways of isolating the effects of geometry on the span efficiency: 1) minimize C_D while holding C_L and Λ fixed, or 2) minimize D while holding L and b fixed. However, neither one of these choices is sufficient to guarantee a unique geometry in an inviscid flow. To appreciate why, consider a lifting-line analysis of an elliptically shaped planform, which will yield a span efficiency of $e = 1$. The aspect ratio and coefficient of lift can be held fixed while the geometry undergoes an isotropic scaling. Thus, there is an infinite family of geometries that meet the constraints and

achieve the same C_D. A similar nonuniqueness arises if we constrain only L and b. By varying the root chord, we can create a set of geometries with elliptical planforms and fixed span, and each geometry in this family can achieve the same lift with an appropriately chosen angle of attack.

Constraining either C_L or L, and any two of b, S, and Λ, is sufficient to produce a unique design. In the studies below, we constrain the span and the reference area. We then choose a lift constraint based on S such that $C_L = 0.375$ for all geometries.

Unless stated otherwise, the reference area is the planform area of the geometry (i.e., the area projected onto the xy-plane). The planform area is calculated using derivatives of the coordinate transformations. For example, suppose the surface coincides with the computational plane $\zeta = 0$. Then the surface area is approximated by

$$S \approx \frac{1}{2} \sum_j \sum_k \left(\frac{|\partial_z \zeta|}{J} \right)_{jk} w_k w_j$$

where J is the Jacobian of the mapping, and the sum is taken over all nodes (j, k) on the surface. Coordinate-mapping derivatives, such as $\partial_z \zeta$, are available from the second-order accurate discretization of the governing equations. The weights w_j and w_k are based on the trapezoid rule, which produces a second-order accurate estimate for S. The integration includes contributions from both sides of a geometry, so the factor of $1/2$ ensures that the resulting surface area is consistent with the projected area for planar geometries. The sensitivities of the surface area with respect to the design variables are calculated analytically.

III. Validation

According to linear aerodynamic theory, an elliptical spanwise lift distribution produces the minimum induced drag when the wake is planar. This provides a challenging benchmark for optimization algorithms, because an order-ϵ perturbation of the elliptical lift distribution produces an order-ϵ^2 perturbation in the induced drag [36]. Hence, obtaining the elliptical lift distribution requires sufficient accuracy in the drag prediction.

Elliptical lift distributions are not unique to one geometry. The same distribution can be obtained using changes in planform, twist, sectional lift, or some combination of these. We first consider twist optimization to recover an elliptical lift distribution; subsequently, we investigate planform optimization.

Both the twist and planform optimizations use the 18 block grid described in Table 1. They also share a common wing geometry and parameterization, which is shown in Fig. 1. The wing geometry has a span of six root-chord units, NACA 0012 airfoil sections, and an initially rectangular planform shape. The wing consists of an inboard section over 97.5% of the semispan and a wing-tip cap over the last 2.5% of the semispan. The upper and lower surfaces of the inboard section are parameterized using 9 B-spline control points in the streamwise direction and 5 to 15 control points in the spanwise direction (white spheres in Fig. 1). The number of spanwise control points is varied to ensure the optimal loading has been achieved.

The wing-tip cap is parameterized using two B-spline patches (upper and lower surfaces) consisting of 9×4 control points in the streamwise and spanwise directions, respectively. The three outboard control points of these patches, shown as dark spheres in Fig. 1, are controlled by the movement of the inboard section such that changes in the cap shape are limited to linear shears.

A. Twist Optimization

For twist optimization, the inboard control-point sections are free to rotate about a fixed trailing edge, i.e., the effective design variables are the local angles of attack. Fixing the trailing edge helps reduce nonplanar effects, although wing-tip edge separation makes a completely planar wake difficult to achieve. The angle of attack is set such that the initial geometry meets the C_L constraint of 0.375, and the projected area is constrained at its initial value of $S = 6$.

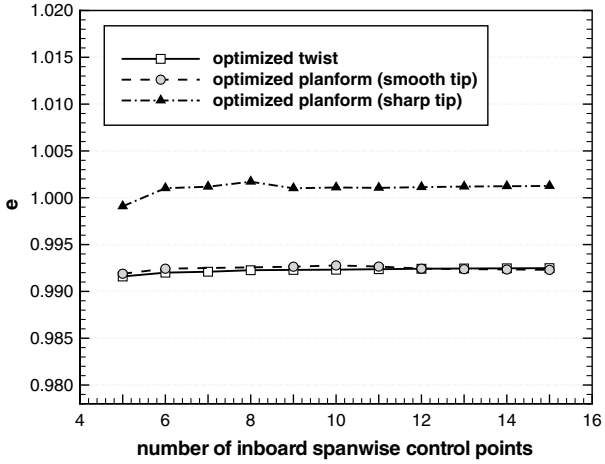

Fig. 2 Span efficiency versus the number of spanwise control points for the twist, smooth-tip planform, and sharp-tip planform optimizations.

Figure 2 plots the span efficiency of the optimally twisted geometries versus the number of spanwise control points on the inboard section. For twist optimization, we see that the span efficiency is relatively constant over the range of spanwise control points considered. With 15 spanwise control points, the span efficiency is approximately $e = 0.993$, in excellent agreement with the lifting-line prediction of $e = 1$.

To confirm the predicted span efficiency, the B-spline mesh corresponding to the 15 spanwise-control-point case was refined by increasing the number of nodes by a factor of 4 in each direction. The resulting grid has the nodal density of the 1152 block grid in Table 1. Using the refined grid, the predicted coefficients of lift and drag are $C_L = 0.37889$ and $C_D = 0.00766$, respectively, and the revised span efficiency is $e = 0.994$. For comparison, the initial untwisted geometry has a predicted span efficiency of $e = 0.978$, based on a refined grid.

Figure 3 shows the spanwise lift distributions of the initial and optimized geometries, for 15 spanwise control points, as well as an elliptical distribution with the same total lift. Recall that all lift distributions are computed using the refined grids. The optimized geometry matches the elliptical distribution closely, except for a small discrepancy visible at the wing tip. This is caused by side-edge separation at the wing tip, which we discuss further in the next section.

The sectional twist angle of the optimized geometry is also shown in Fig. 3. The twist does not match the elliptical twist predicted by

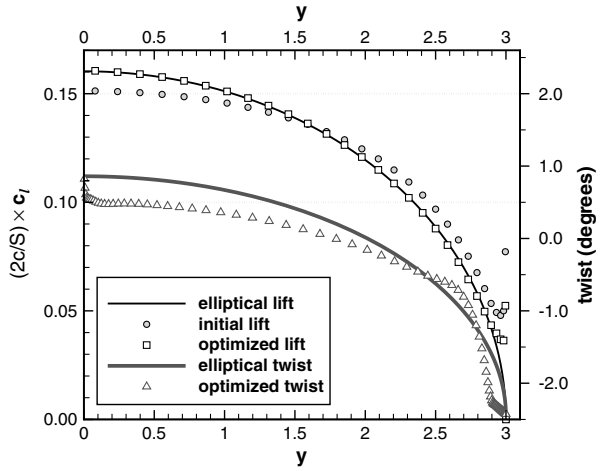

Fig. 3 Lift distributions of the initial and optimized geometries (15 spanwise control points) compared with an elliptical distribution with the same total lift: the sectional twist (in degrees) of the optimized geometry is also included.

linear theory. For comparison, we created a geometry with a prescribed twist that closely approximates an elliptical twist distribution; an exact elliptical curve is not possible using B-splines. The mean error in approximating an elliptical twist with the given parameterization is 0.047° or 1.4% based on the difference between the root and tip twist angles. The optimization algorithm was applied to the prescribed geometry to find the angle of attack necessary to meet the lift constraint of $C_L = 0.375$. With this angle of attack, the span efficiency is predicted to be $e = 0.991$.

Subsequently, the grid for the prescribed-twist geometry was refined by a factor of 4. On the refined grid, we find $C_L = 0.37895$ and $C_D = 0.00767$ for this geometry. This yields a span efficiency of $e = 0.993$, which is smaller than the value obtained for the optimized geometry on its refined mesh, i.e., the induced drag is larger on the geometry with the prescribed twist. Consider the lift distribution for the prescribed-twist geometry, which is plotted in Fig. 4. The figure shows that the lift distribution from the prescribed geometry does not match the elliptical lift distribution as closely as the one produced by the optimized geometry.

B. Planform Optimization

Planform shape can also be manipulated to produce an elliptical lift distribution. Indeed, many introductions to lifting-line theory focus on elliptical planform shapes. By including the effects of wake geometry, Smith and Kroo [8] have shown that the planform may not be exactly elliptical, depending on the shape of the trailing edge. For example, a curved trailing edge will produce a nonplanar wake for nonzero angles of attack, so the elliptical lift distribution will no longer be optimal. This suggests that we use a straight trailing edge perpendicular to the symmetry plane.

With a planar trailing edge, we might expect to recover a crescent-shaped wing [7,8]. However, as we shall see, the optimal planform shape depends subtly on the wing-tip shape. In particular, the tip geometry can trigger side-edge separation, which leads to a nonplanar wake. To illustrate this effect, we consider two tip geometries; one that has a smooth edge and one that has a sharp edge.

The initial planform is rectangular, and the leading-edge control points of the inboard B-spline patches are free to move in the x-direction (streamwise). As discussed above, the trailing-edge control points are fixed to reduce the effects of a nonplanar wake. The remaining control points in each section are scaled based on the chord length; hence, the effective design variables are the chord lengths at the spanwise stations.

The projected area is constrained by its initial value of $S = 6$. This constraint ensures a consistent reference area, and it prevents nonunique optima that would arise with a variable angle of attack; there is an optimal planform for each angle of attack. The target lift coefficient is 0.375.

Figure 2 shows the optimized span efficiencies for the smooth-tip and sharp-tip geometries using 5 to 15 spanwise control points. The optimization runs for the smooth-tip planform using 7 and 8 spanwise control points failed to converge and are not included in the figure. The span efficiency of the smooth-tip planform is relatively insensitive to the number of spanwise points and matches the span efficiency of the twist optimization ($e = 0.992$ for 15 spanwise control points). In contrast, the sharp-tip planform has a span efficiency that is almost 1% higher ($e = 1.001$ for 15 spanwise control points).

Using grids with 88 million-nodes (Table 1), refinement studies of the planforms with 15 spanwise control points yield $e = 0.988$ for the smooth-tip planform and $e = 0.997$ for the sharp-tip planform. This suggests the performance differences between the two planforms is real and not due to numerical errors.

The optimal planform shapes are plotted in Fig. 5. Only the planforms corresponding to 15 spanwise control points are shown, since the geometries with 11 through 15 points are similar. The two wing-tip shapes lead to similar planforms over most of the span; however, the two planforms differ toward the wing tip, where the smooth-tip planform has a monotonically decreasing chord, and the sharp-tip planform has an abrupt increase in the chord.

The two optimal planform shapes are clearly not elliptical. More important, their lift distributions are not elliptical, as Fig. 6 demonstrates. Liersch et al. [14] found that an elliptical planform does not achieve the theoretical minimum induced drag, unless a twist is also applied. While this may explain why the present planforms are not elliptical, it does not adequately explain why the lift distributions are not elliptical.

Side-edge separation provides a possible explanation for the nonelliptical lift distributions and the distinct planform shapes at the tip. On the sharp-tip planform the vortex releases along the wing tip near the leading edge and curls onto the upper side of the wing, as shown in Fig. 7. The flowfield created by the vortex lowers the pressure on the upper surface near the tip, similar to the vortices on a delta-wing. Evidence for this effect is visible in the lift distributions in Fig. 6, as well as the experimental results of [33]. On the smooth-tip planform the tip vortex also releases along the wing tip, but much closer to the trailing edge.

As the wing-tip chord decreases, the region of reduced pressure also decreases; hence, there appears to be a tradeoff between maintaining this vortex-induced low-pressure region and establishing an elliptical lift distribution. The wake offers an alternative perspective. The edge separation produces a nonplanar wake, and the vertical extent of this wake is increased by extending the chord at the tip (a tip with finite chord has a vertical component when the wing is inclined at an angle of attack). This is also illustrated in Fig. 7. The sharp-tip planform is able to exploit the resulting nonplanar wake more than the smooth-tip planform.

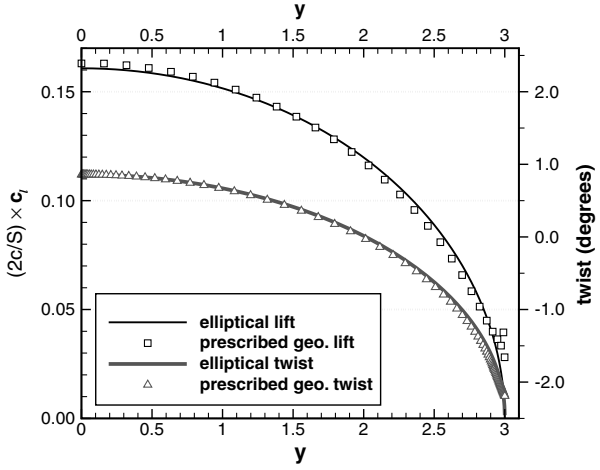

Fig. 4 Lift and twist distributions for a geometry with a prescribed twist that is approximately elliptical.

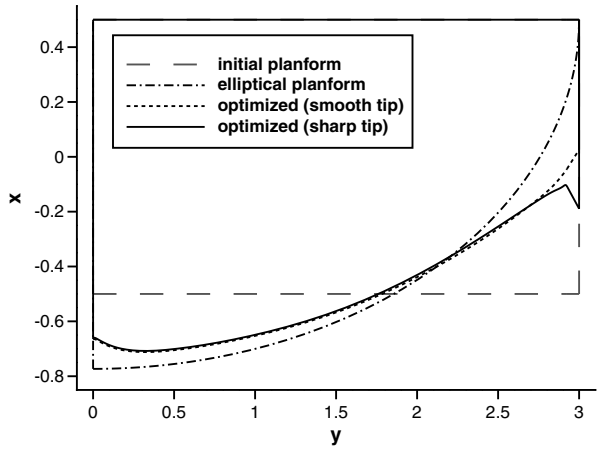

Fig. 5 Initial and optimal planform semispan shapes (axes are not to scale).

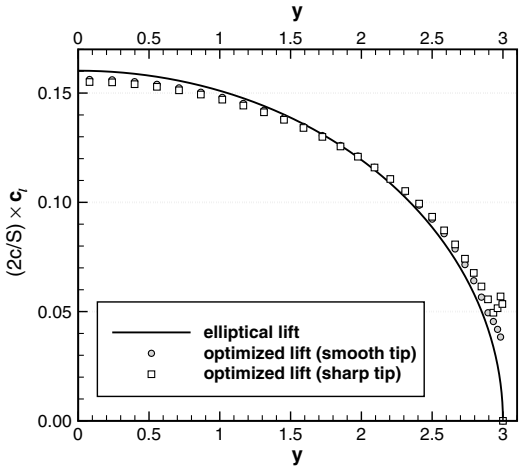

Fig. 6 Elliptical lift distribution and the predicted lift distribution of the two optimized planform geometries.

IV. Winglets

In [15], it was shown that a gradient-based aerodynamic shape optimization is capable of recovering winglets from an initially planar wing. However, the number of spanwise degrees of freedom in that study was insufficient to obtain the optimal lift distribution, so in this section we investigate the optimal loading for winglets more thoroughly. In particular, we are interested in comparing the results of aerodynamic shape optimization to those of linear theory.

The initial winglet semispan geometry is shown in Fig. 8. Although the figure depicts a winglet-up geometry, both winglet-up and winglet-down orientations are considered. The span is approximately 6 chord units and the winglet height is approximately 0.6 chord units. NACA 0012 sections are used throughout the span of the geometry except toward the winglet tip where the thickness-to-chord ratio is gradually reduced.

The geometry is parameterized using 16 B-spline patches: 4 patches on the lower surface of the main wing, 4 patches on the upper surface of the main wing, 4 patches on the outer surface of the winglet, and 4 patches on the inner surface of the winglet. Each patch consists of 6 control points in the streamwise direction. The number of control points in the spanwise or vertical direction is varied from 4 to 8, to ensure the optimal loading has been obtained. Therefore, five separate optimization runs are considered, with 13, 17, 21, 25, and 27 total spanwise-vertical control points (accounting for the common set of control points shared along each patch edge). The geometry in Fig. 8 corresponds to the parameterization with 6×8 control points per patch, or 27 total spanwise-vertical control points.

The main wing and winglet control-point sections are free to rotate about axes parallel to the y-axis and z-axis, respectively. The sections are constrained to have the same chord length as the root section, which is permitted to vary. The y-coordinate of each section in the main wing is linearly interpolated between the root and winglet junction. Similarly, the z-coordinate of each section in the winglet is interpolated between the junction and the winglet tip.

The x-coordinate of the leading edge is fixed at $x = -0.5$, and the control point coordinates are subject to the bound constraints $|z| \leq 0.3$ and $|y| \leq 3$. Because the bound constraints are applied to the control-point coordinates, the convex-hull property of B-spline curves prevents the surface geometry from touching the bound constraints. Applying the bounds directly to the surface nodes would significantly increase the size of the optimization problem.

The control points along the junction between the main wing and winglet are determined by the positions of adjacent control points: the x and y coordinates match those of control points on the winglet, while the z coordinates are taken from points on the main wing.

Along the winglet tip, the control-point coordinates are interpolated between the leading and trailing edge. In addition, the leading- and trailing-edge control-point coordinates at the tip are extrapolated from the positions of the two inboard control points; this is necessary to prevent excessive deflections at the wing tip.

The maximum anhedral angle between any two adjacent control points on the main wing is 35°. Similarly, the maximum dihedral angle between adjacent control points on the winglet is 125°. These

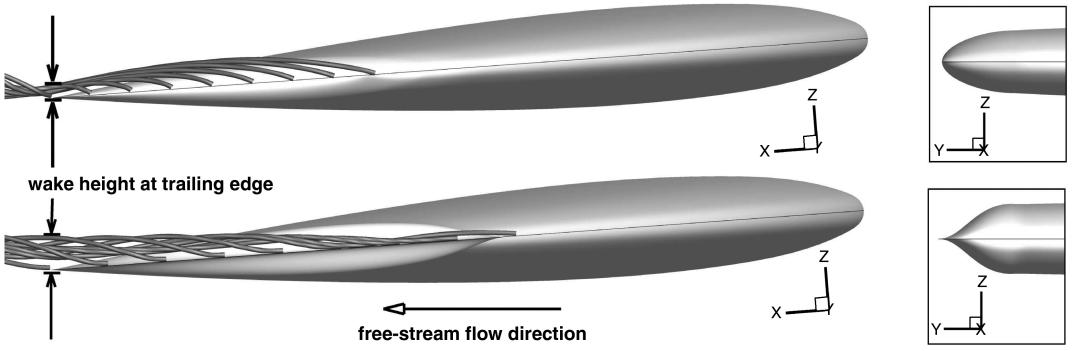

Fig. 7 Wing tip view of the optimized smooth-tip planform (upper) and optimized sharp-tip planform (lower) with the tip vortices visualized with streamlines.

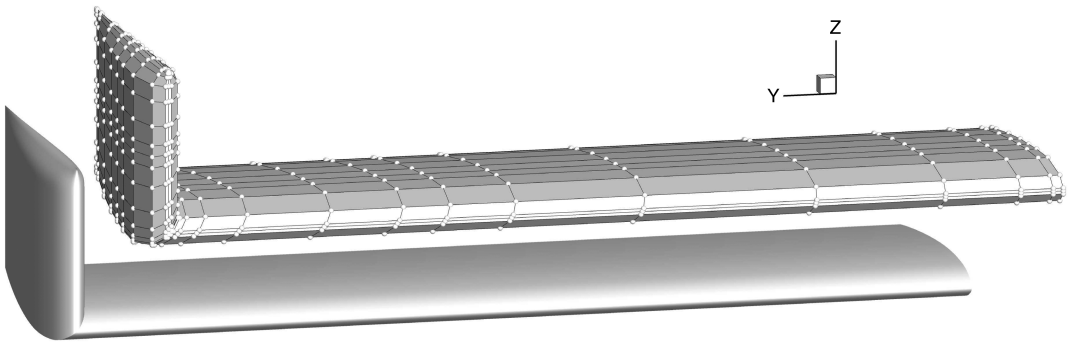

Fig. 8 Initial B-spline control mesh (upper) and surface geometry (lower) for the winglet optimization.

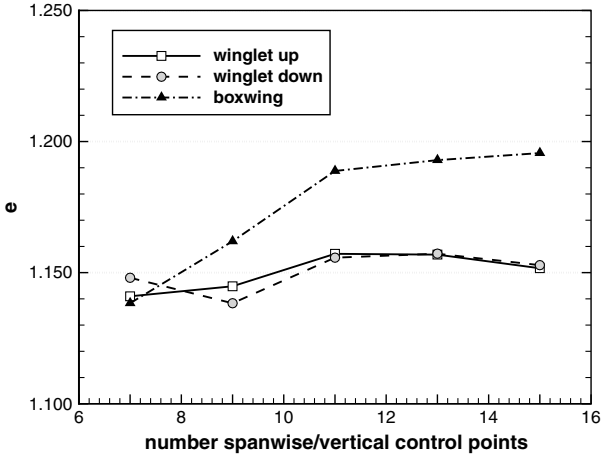

Fig. 9 Span efficiency versus the number of spanwise control points for the optimized winglet-up, winglet-down, and box-wing geometries.

constraints are necessary to prevent invalid geometries and meshes near the winglet junction, a problem that we elaborate on below.

The 48-block grid from Table 1 is used for all optimization runs. As usual, the coefficient of lift is constrained at 0.375 and an equality constraint of $S = 6$ is imposed on the projected area.

Figure 9 plots the span efficiency of the optimized winglet-up and winglet-down geometries as a function of the number of spanwise control points over the main wing (or vertical control points over the winglet). The figure also plots the span efficiency of the box-wing geometry, which is described in the next section. As the control point density increases, the span efficiency appears to plateau between $e = 1.15$ and $e = 1.16$ for both winglet orientations.

The optimized winglet-up geometry corresponding to 15 spanwise control points is illustrated in Fig. 10. A similar illustration of the optimal winglet-down geometry is given in Fig. 11. Observe that the trailing edge at the junction stretches toward the corner of the bound constraints, which are illustrated with dashed lines in the inset figures. The optimization attempts to maximize the vertical distance between the junction edge and the tip, but this appears to conflict with the optimal twist near the junction. Consequently, the trailing edge of the wing and winglet approach one another, necessitating the constraints on dihedral discussed earlier.

To confirm the span efficiency values, the 48-block grids from the optimized 13 spanwise-control-point parameterizations were refined by a factor of 3 and subdivided into 1296 blocks; see Table 1 for the grid statistics. Using these refined grids, we obtain $e = 1.147$ for the winglet-up geometry and $e = 1.145$ for the winglet-down geometry.

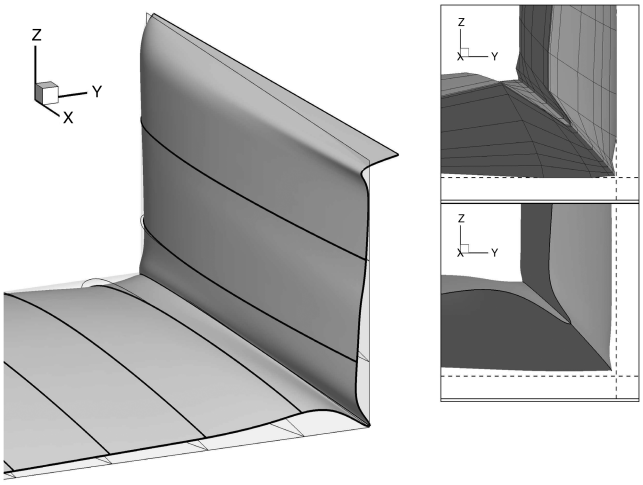

Fig. 10 Optimized winglet-up geometry and transparaent initial geometry viewed from downstream; inset figures show close-up of the B-spline control points (upper) and surface (lower) at the winglet junction.

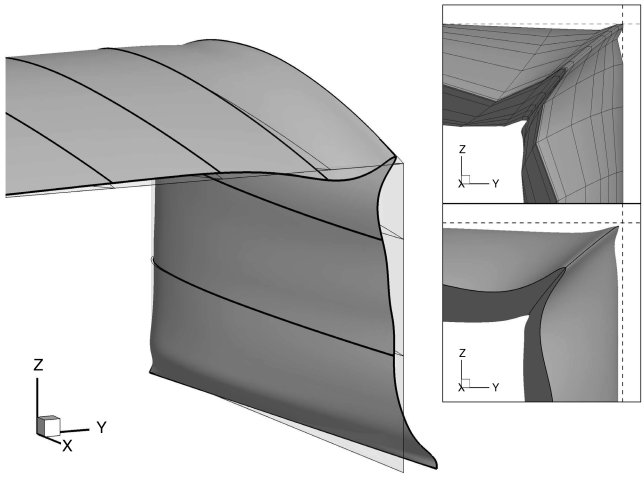

Fig. 11 Optimized and initial (transparent) winglet-down geometries viewed from downstream, with inset figures showing close-up of the B-spline control points (upper) and surface (lower) at the winglet junction.

How do these results compare with linear theory? If we model a winglet-up configuration using horizontal and vertical lifting lines that coincide with the bound constraints (height-to-span ratio of 0.1), we find that the optimal span efficiency is approximately $e = 1.24$. This is significantly larger than the value predicted by the nonlinear solver. The difference can be largely explained by a tacit assumption made in our application of linear theory. The lifting line can be considered the wake at the trailing edge; therefore, in obtaining the lifting-line result we have maximized the span and vertical height of the trailing edge, while neglecting the bound constraints on the rest of the geometry.

The trailing edge of the initial geometry provides a more realistic lifting-line shape for a comparison with linear theory, because the complete geometry is contained within the bound constraints. Using this trailing edge, which has a height-to-span ratio of 0.09 rather than 0.1, the optimal span efficiency predicted by linear theory is $e = 1.17$, in much closer agreement with the nonlinear results.

Finally, we note that the two winglet orientations have very similar span efficiencies; however, this is not universally true for all winglets. Bourdin [11] notes that the optimal winglet orientation is a function of the tip geometry, which controls the location where the tip vortex is shed and, consequently, the vertical extent of the wake. For example, Bourdin found that a winglet-up geometry outperforms a winglet-down geometry when the tip is swept forward, and he found the converse when the tip is swept back.

V. Box Wing

The box-wing configuration is a closed-wing system that resembles a biplane with a vertical surface joining the wing tips. The vertical connection creates a continuous lifting surface and eliminates the wing tips. Indeed, the absence of wing tips is the distinguishing feature of closed-wing systems. While they do not eliminate induced drag, closed-wing systems reduce it significantly. For example, according to linear theory, the box wing produces the minimum induced drag for a given height-to-span ratio [37].

In this section, our objective is to find the minimum induced drag for a box-wing configuration and compare this Euler-based result with linear theory. Thus, this study is analogous to the previous study of the winglet.

The box-wing geometry has a span of 6 chord units and a maximum height of 0.6 chord units. We use a sectional shape that approximates the NACA 0012 airfoil. The semispan configuration is parameterized using 24 B-spline patches. The vertical end plate and two horizontal semispan wings use 8 patches each: 4 each for the inner and outer surfaces. The patches consist of 6 control points in the streamwise direction and 4 to 8 points in the spanwise or vertical direction. As with the previous cases, varying the spanwise control-point density ensures the optimal loading has been achieved.

Sections along the horizontal wings are permitted to rotate about axes parallel to the y-axis. Similarly, sections along the vertical end plate are free to rotate about axes parallel to the z-axis. Each section is constrained to have the same (variable) chord length. The y-coordinate of each section in the horizontal wings is linearly interpolated between the root and junction. The z-coordinate of each section in the end plate is interpolated between the upper and lower junctions. The leading edge is fixed in the streamwise direction at $x = -0.5$, and the control point coordinates are subject to the bound constraints $|z| \leq 0.3$ and $|y| \leq 3$.

At the upper and lower junctions, where the horizontal wings join the end plate, the control point coordinates are extrapolated from adjacent sections. The x and y coordinates along the junction are equal to the coordinates of the adjacent control points on the end plate, and the z coordinates are equal to the coordinate values of adjacent control points on the main wing.

As with the winglet, some constraints on the local dihedral are necessary to prevent invalid geometries and meshes near the junctions. On the lower wing, adjacent spanwise control points are limited to a maximum anhedral angle of 35°. Conversely, adjacent spanwise control points on the upper wing are limited to a maximum dihedral angle of 35°. Finally, the dihedral angle between adjacent control points on the winglet must lie between 55 and 125°.

The 48-block canonical grid from Table 1 is used during the optimizations. As in the previous studies, the projected area is constrained at $S = 6$, and the coefficient of lift is fixed at $C_L = 0.375$.

The span efficiency as a function of the number of spanwise (or vertical) control points is plotted in Fig. 9. Although there is a significant increase from 7 to 11 spanwise control points, the efficiency stabilizes between $e = 1.19$ and $e = 1.20$ for the larger control-point densities. A refinement study based on the 15-spanwise-control-point geometry and the 1296-block grid from Table 1 yields a span efficiency of $e = 1.16$.

Figure 12 shows coefficient of pressure contours around the optimized box-wing geometry (15 spanwise control points). The inset figure compares the trailing-edge shape of the optimized geometry with the initial geometry. As with the winglet configurations, the junctions are pushed toward the corners of the bound constraints to maximize the span and vertical extent of the wake.

According to linear theory, a box wing modeled as a lifting line with a height-to-span ratio of 0.1 has a span efficiency of $e = 1.27$; however, like the linear analysis of the winglet, this naively applies the bound constraints to the trailing edge and not the entire geometry. When we account for the airfoil thickness, we obtain a more realistic height-to-span ratio of 0.0816 and a lifting line analysis produces $e = 1.18$. This prediction agrees well with the nonlinear optimization results.

We close this section with some remarks on the optimal loading of closed systems. According to linear theory, a vortex loop of constant circulation can be added to the bound vortex of a closed system without changing the induced drag [1]. In the context of lifting-line theory, this implies that a box-wing configuration of minimum induced drag is not unique. It is not clear if this nonuniqueness is present in the Euler-based solution. The nonlinear physics may eliminate the nonuniqueness, or small numerical errors may isolate one geometry as a local minimum in the design space. Further investigation is necessary to determine the relative impact of these two factors.

VI. Split Tip

In [9], Smith studied a split-tip configuration consisting of a main wing with two tip wings. The configuration provides a simple model for tip sails, which have been studied experimentally by Spillman [38], for example (see also [39]). In Smith's geometry, the tip wings are staggered in the streamwise direction, and the rear tip wing is swept back. Although his split-tip configuration has a planar wake at zero angle of attack, the streamwise separation of the tip wings produces a nonplanar wake when the wing is inclined to the flow. Smith showed that a linear discrete-vortex method predicts that the split-tip configuration has a span efficiency of approximately $e=$ 1.066, at an angle of attack of 9 deg ($C_L = 0.761$), i.e., a drag reduction of over 6%. He also analyzed the configuration using a nonlinear, force-free wake calculation. When nonlinear effects were included, the split tip reduced the drag by 10% relative to an elliptical lift distribution. Smith's experimental studies confirmed this reduction.

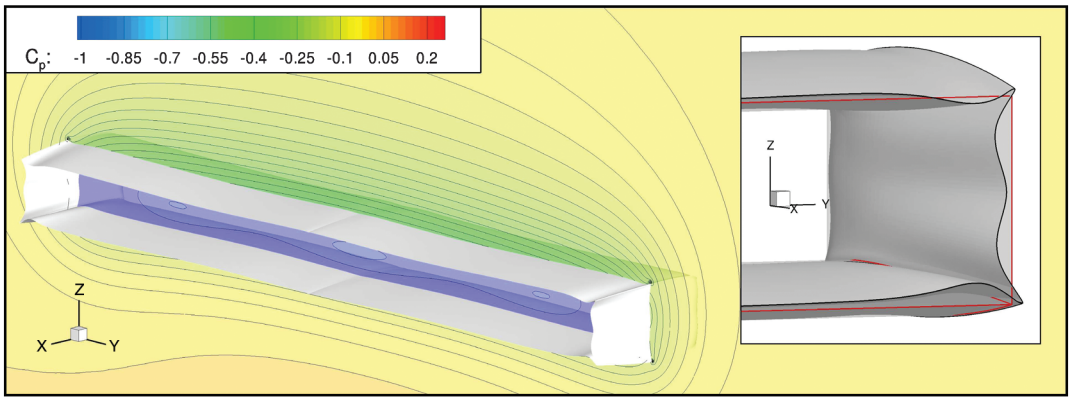

Fig. 12 Optimized box-wing configuration with coefficient of pressure contours on the plane $x = 0$, and inset showing the trailing-edge shape of the optimized and initial (transparent) configurations.

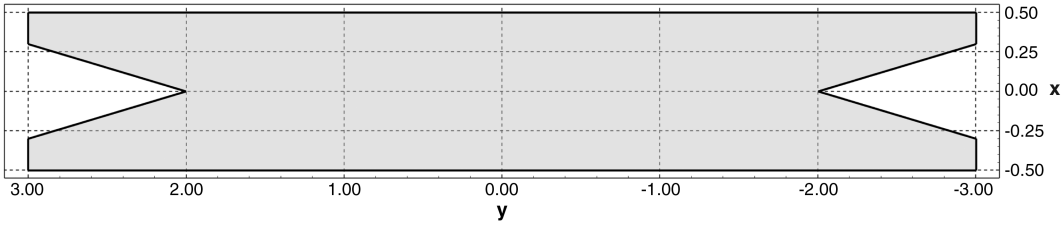

Fig. 13 Planform shape of the split-tip configuration.

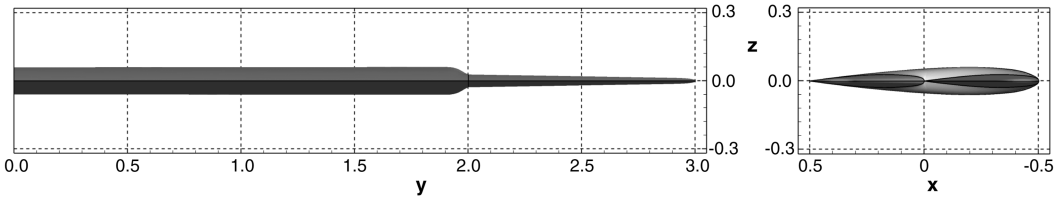

a) Baseline split-tip configuration

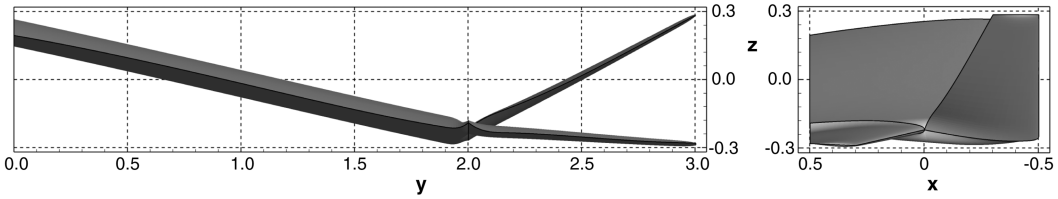

b) up-down split-tip configuration

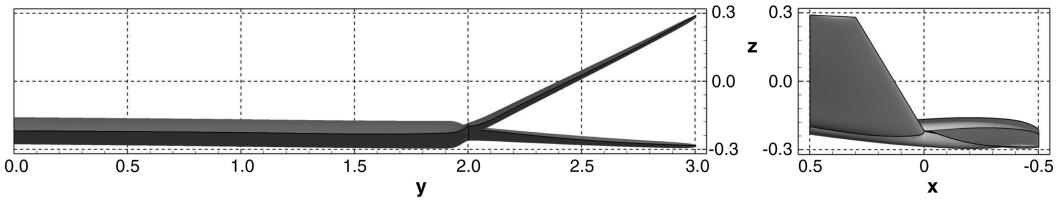

c) down-up split-tip configuration

Fig. 14 Optimal split-tip geometries.

Motivated by Smith's results, we consider the effect of dihedral on the induced drag of a split-tip configuration. The hope is that an optimized nonplanar split-tip, like its planar analog, will yield a span efficiency larger than the value predicted by linear theory.

The initial split-tip configuration is similar to Smith's geometry. The main wing has a rectangular planform, while the tip wings have taper ratios of 0.4. The semispan is three chord lengths, and the junction between the main wing and tip wings is located at two-thirds of the semispan. The projected/reference area is $S = 5.4$. The main wing and tip wings have NACA 0012 sections throughout most of the span, with some fairing required at the junction and at the wing tips. The trailing edge of the rear tip wing has no sweep, and the planform is symmetric about the midchord (in contrast with Smith's geometry). Figure 13 shows the planform shape of the split tip.

The canonical grid for the split-tip configuration is the 42-block grid listed in Table 1. Each block in the grid is a B-spline volume

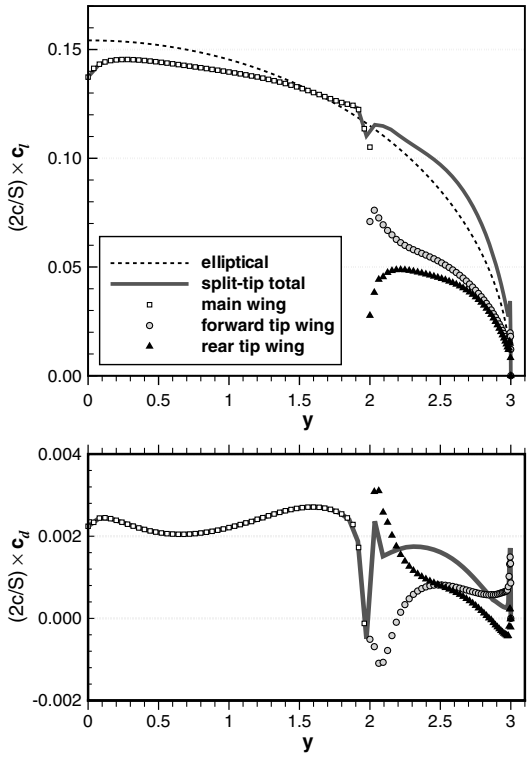

Fig. 15 Lift and drag distributions for the up-down split-tip configuration.

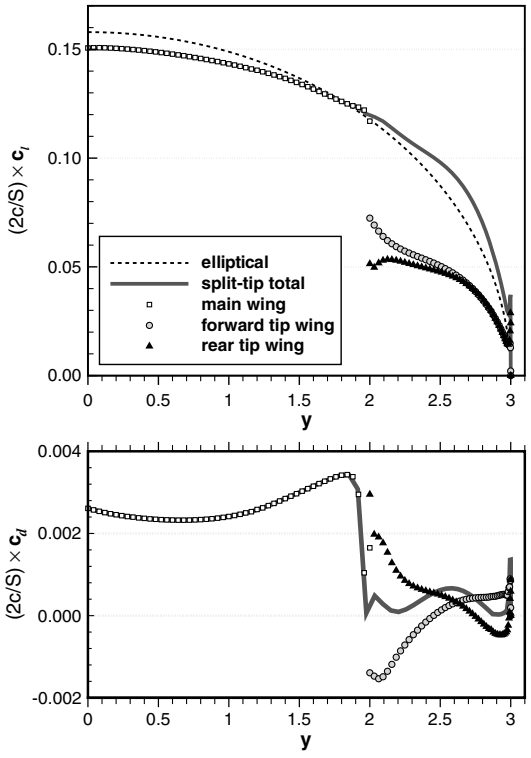

Fig. 16 Lift and drag distributions for the down-up split-tip configuration.

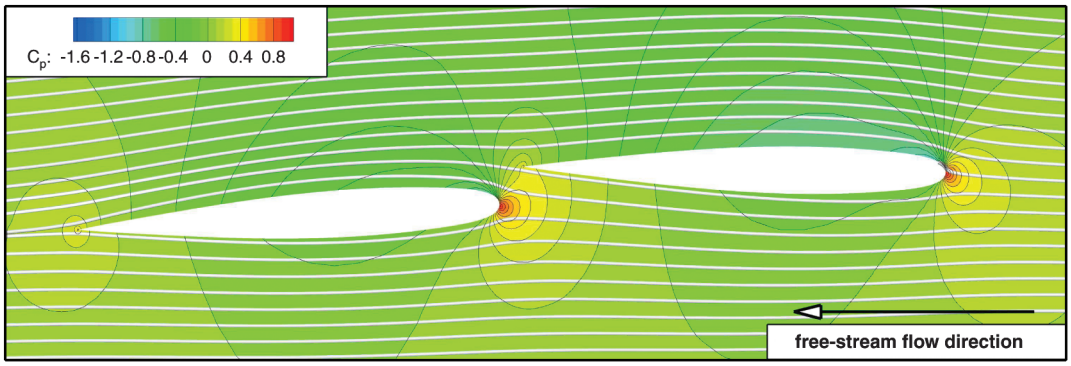

Fig. 17 Flow visualization on the plane $y = 2.1$ for the up-down split-tip configuration. Streamlines are computed using the velocity field $(u, 0, w)$ to illustrate the projected velocity direction. Contours of the coefficient of pressure are also shown. The tip wings are twisted to take advantage of the local flow direction.

consisting of $6 \times 6 \times 5$ control points. The semispan geometry is composed of four B-spline patches on the upper surface (two for the main wing and one each for the tip wings), and four patches on the lower surface. Each patch is parameterized with 6×6 control points: we consider only one set of spanwise control points.

The leading edges of the main and tip wings are limited to linear variations in spanwise camber, but each section is free to rotate parallel to the xz plane. Thus, twist can be used to optimally load the configuration. The chord length of each section is constrained such that it maintains a constant ratio with the root chord. The control points are constrained by the bound constraint $|z| \leq 0.3$. Allowing the configuration to translate introduces nonunique designs, but any design that activates both the upper and lower bound constraints will be unique.

Figure 14 shows two local optima obtained from the split-tip optimization. The split-tip optimum in Fig. 14b was obtained from the initial configuration shown in Fig. 14a. We will refer to this optimum as the up–down configuration, as a mnemonic for the positions of the forward and rear tip-wing dihedrals. Similarly, we refer to the local optimum shown in Fig. 14c as the down–up configuration. The optimization leading to the down–up configuration was initiated by giving the forward and rear tips on the baseline geometry dihedral angles of $-19.7°$ and 19.7, respectively. We also considered initial geometries with both tip wings up and both tip wings down, in an attempt to identify additional local optima. Both of these initial geometries lead to the up–down configuration; nevertheless, this does not preclude the existence of distinct local optima for this parameterization.

Both split-tip optima have maximized the vertical distance between the tip wings. The up-down configuration has a predicted induced drag of $C_D = 0.00580$ ($e = 1.158$), while the down–up configuration has a predicted value of $C_D = 0.00585$ ($e = 1.148$). For the refinement study, we increased the nodal resolution by a factor of 3 in each coordinate direction. The refined grid for the up–down configuration yields $C_L = 0.3762$, $C_D = 0.00579$, and a span efficiency of $e = 1.167$. The improved estimates for the down–up configuration are similar: $C_L = 0.3763$, $C_D = 0.00583$, and $e = 1.160$. These span efficiencies are comparable with or exceed that of the box wing.

We can gain some insight into the efficiency of the split-tip configurations by examining their spanwise distributions of lift and drag. Figure 15 plots these distributions for the up–down configuration, and shows the individual contributions from the main and tip wings. Figure 16 contains the analogous plots for the down-up configuration. The lift distributions reveal that the outer load is roughly shared by the tip wings. The drag distribution is even more interesting, since it reveals that the tip wings are producing thrust over sections of their span. This is precisely the goal of well-designed tip sails [38]. For example, near $y = 2$ the upwash from the trailing tip wing creates a localized flow for the forward tip wing that increases the effective angle of attack; see Fig. 17. The optimization algorithm has produced a geometry that exploits this effect automatically.

The maximum height-to-span ratio along the trailing edge of the up-down split-tip is 0.093. Based on this ratio, a linear lifting-curve analysis of a simplified split-tip configuration produces $e = 1.17$. Once again, the agreement between linear theory and the Euler-based optimization is good: there is no significant performance improvement as observed for Smith's planar split-tip. For the present split-tip geometries, the nonlinear effects will be reduced by the increased vertical separation between the tip vortices, and this may explain the absence of drag reduction beyond the predictions of linear theory. Nevertheless, the split-tip still performs favorably compared with the box-wing, because the split-tip is better able to maximize the height-to-span ratio of the wake.

VII. Conclusions

Table 2 summarizes the predicted span efficiencies and force coefficients of the configurations studied herein. The results listed are those obtained from the refined grids, and the number of nodes and surface-node spacing are included in the table for reference (see Table 1 for further details regarding the grids and the definition of surface node spacing).

The optimization studies have revealed several interesting results regarding induced drag, which are listed below. We emphasize that these conclusions may only apply to inviscid flows. In addition, the chosen parameterizations may have limited the designs in some

Table 2 Summary of the induced drag minimization studies ordered by increasing span efficiency (results from refined grids)

Configuration	e	C_L	C_D	S	Grid nodes	Surface spacing
Smooth-tip planform	0.988	0.37829	0.00769	6.0	88 387 200	0.0070
Twist	0.994	0.37889	0.00766	6.0	88 387 200	0.0070
Sharp-tip planform	0.997	0.37850	0.00762	6.0	88 387 200	0.0070
Winglet-down	1.146	0.37563	0.00653	6.0	152 473 104	0.0060
Winglet-up	1.147	0.37471	0.00649	6.0	152 473 104	0.0060
Box wing	1.151	0.37482	0.00647	6.0	152 473 104	0.0060
Split tip down–up	1.160	0.37634	0.00583	5.4	103 335 750	0.0062
Split tip up–down	1.167	0.37627	0.00579	5.4	103 335 750	0.0062

cases, and increased geometric flexibility may improve the predicted performance of these configurations.

1) An elliptical planform does not produce the minimum induced drag when wing-tip edge separation is present. The edge separation leads to a nonplanar wake, which can be exploited to reduce the vortex drag if the wing tip has a finite chord-length.

2) The span efficiency of the optimized twist and planform geometries was found to be relatively insensitive to the number of spanwise degrees of freedom. In contrast, the winglet and box-wing configurations required at least 11 nonuniformly spaced spanwise control points to achieve the optimal loading.

3) When comparing the results of an Euler-based optimization with linear theory, the bound constraints must be carefully adapted. Applying identical bound constraints to the lifting line neglects the finite-thickness of wings and winglets, and this effectively increases the span and/or height of the wing.

4) Bound constraints on the winglet and box-wing geometries lead to a tradeoff between the optimal twist and maximizing the span and height of the wake.

5) For the same spanwise and vertical bound constraints, an optimized split-tip geometry was found to outperform an optimized box-wing geometry by approximately 1.5%. The split-tip geometry achieves a larger height-to-span ratio for the wake, because its thin tips are less impacted by the bound constraints. Nonlinear effects do not appear to play a significant role in the induced drag of the nonplanar split-tip.

The present findings are interesting, but they are ultimately limited by the inviscid assumption. Therefore, future work will consider viscous and turbulent effects in exploratory aerodynamic shape optimization of nonplanar geometries. Extension to aerostructural optimization will also be pursued.

Acknowledgments

The authors gratefully acknowledge financial assistance from Bombardier Aerospace, the Natural Sciences and Engineering Research Council, the Canada Research Chairs program, Mathematics of Information Technology and Complex Systems, and the University of Toronto. All results were obtained on the high-performance computing resources of the SciNet Consortium.

References

[1] Kroo, I., "Drag Due to Lift: Concepts for Prediction and Reduction," *Annual Review of Fluid Mechanics*, Vol. 33, No. 1, 2001, pp. 587–617. doi:10.1146/annurev.fluid.33.1.587

[2] Munk, M., "The Minimum Induced Drag of Aerofoils," NACA Technical Rept. No. 121, 1921.

[3] Cone, C. D. J., "The Theory of Induced Lift and Minimum Induced Drag of Nonplanar Lifting Systems," NASA TR R-139, 1962.

[4] Mangler, W., "The Lift Distribution of Wings with End Plates," NACA Technical Rept. No. 856, Originally Published as "Die Auftriebsverteilung am Tragflugel mit Endscheiben," 1938.

[5] Lundry, J. L., and Lissaman, P. B. S., "A Numerical Solution for the Minimum Induced Drag of Nonplanar Wings," *Journal of Aircraft*, Vol. 5, No. 1, 1968, pp. 17–21. doi:10.2514/3.43901

[6] Lowson, M. V., "Minimum Induced Drag for Wings with Spanwise Camber," *Journal of Aircraft*, Vol. 27, No. 7, July 1990, pp. 627–631. doi:10.2514/3.25332

[7] van Dam, C., "Induced-Drag Characteristics of Crescent-Moon-Shaped Wings," *Journal of Aircraft*, Vol. 24, No. 2, 1987, pp. 115–119. doi:10.2514/3.45427

[8] Smith, S. C., and Kroo, I. M., "Computation of Induced Drag for Elliptical and Crescent-Shaped Wings," *Journal of Aircraft*, Vol. 30, No. 4, 1993, pp. 446–452. doi:10.2514/3.46365

[9] Smith, S. C., "A Computational and Experimental Study of Nonlinear Aspects of Induced Drag," NASA TP 3598, 1996.

[10] Eppler, R., "Induced Drag and Winglets," *Aerospace Science and Technology*, Vol. 1, No. 1, 1997, pp. 3–15. doi:10.1016/S1270-9638(97)90019-5

[11] Bourdin, P., "Étude Théorique et Numérique des Effets d'Extrémité de Volilure sur la Traînée Induite," Ph.D. Thesis, Université de Poitiers, Poitiers, France, 2003.

[12] Phillips, W. F., Fugal, S. R., and Spall, R. E., "Minimizing Induced Drag with Wing Twist, Computational Fluid Dynamics Validation," *Journal of Aircraft*, Vol. 43, No. 2, 2006, pp. 437–444. doi:10.2514/1.15089

[13] Yamazaki, W., Matsushima, K., and Nakahashi, K., "Aerodynamic Design Optimization Using the Drag-Decomposition Method," *AIAA Journal*, Vol. 46, No. 5, May 2008, pp. 1096–1106. doi:10.2514/1.30342

[14] Liersch, C. M., Streit, T., and Visser, K. D., "Numerical Implications of Spanwise Camber on Minimum Induced Drag Configurations," *47th AIAA Aerospace Science Meeting and Exhibit*, AIAA Paper 2009-898, Jan. 2009.

[15] Hicken, J. E., and Zingg, D. W., "Aerodynamic Optimization Algorithm with Integrated Geometry Parameterization and Mesh Movement," *AIAA Journal*, Vol. 48, No. 2, Feb. 2010, pp. 400–413. doi:10.2514/1.44033

[16] Kreiss, H.-O., and Scherer, G., "Finite Element and Finite Difference Methods for Hyperbolic Partial Differential Equations," *Mathematical Aspects of Finite Elements in Partial Differential Equations*, edited by C. de Boor, Academic Press, New York, 1974.

[17] Strand, B., "Summation by Parts for Finite Difference Approximations for D/DX," *Journal of Computational Physics*, Vol. 110, No. 1, 1994, pp. 47–67. doi:10.1006/jcph.1994.1005

[18] Carpenter, M. H., Gottlieb, D., and Abarbanel, S., "Time-Stable Boundary Conditions for Finite-Difference Schemes Solving Hyperbolic Systems: Methodology and Application to High-Order Compact Schemes," *Journal of Computational Physics*, Vol. 111, No. 2, 1994, pp. 220–236. doi:10.1006/jcph.1994.1057

[19] Carpenter, M. H., Nordström, J., and Gottlieb, D., "Revisiting and Extending Interface Penalties for Multi-Domain Summation-by-Parts Operators," *Journal of Scientific Computing*, June 2009, pp. 1–33.

[20] Carpenter, M. H., Nordström, J., and Gottlieb, D., "A Stable and Conservative Interface Treatment of Arbitrary Spatial Accuracy," *Journal of Computational Physics*, Vol. 148, No. 2, 1999, pp. 341–365. doi:10.1006/jcph.1998.6114

[21] Saad, Y., and Sosonkina, M., "Distributed Schur Complement Techniques for General Sparse Linear Systems," *SIAM Journal on Scientific Computing*, Vol. 21, No. 4, 1999, pp. 1337–1357. doi:10.1137/S1064827597328996

[22] Hicken, J. E., and Zingg, D. W., "Globalization Strategies for Inexact-Newton Solvers," *19th AIAA Computational Fluid Dynamics Conference*, AIAA Paper 2009-4139, June 2009.

[23] Hicken, J. E., and Zingg, D. W., "A Parallel Newton–Krylov Solver for the Euler Equations Discretized Using Simultaneous Approximation Terms," *AIAA Journal*, Vol. 46, No. 11, Nov. 2008, pp. 2773–2786. doi:10.2514/1.34810

[24] Gill, P. E., Murray, W., and Saunders, M. A., "SNOPT: An SQP Algorithm for Large-Scale Constrained Optimization," *SIAM Journal on Optimization*, Vol. 12, No. 4, 2002, pp. 979–1006. doi:10.1137/S1052623499350013

[25] Hicken, J. E., and Zingg, D. W., "A Simplified and Flexible Variant of GCROT for Solving Nonsymmetric Linear Systems," *SIAM Journal on Scientific Computing*, Vol. 32, No. 3, 2010, pp. 1672–1694. doi:10.1137/090754674

[26] Smith, S. C., and Kroo, I. M., "Induced Drag Computations on Wings with Accurately Modeled Wakes," *Journal of Aircraft*, Vol. 34, No. 2, 1997, pp. 253–255. doi:10.2514/2.7570

[27] van Dam, C. P., and Nikfetrat, K., "Accurate Prediction of Drag Using Euler Methods," *Journal of Aircraft*, Vol. 29, No. 3, 1992, pp. 516–519. doi:10.2514/3.46194

[28] van Dam, C. P., Nikfetrat, K., Wong, K., and Vijgen, P. M. H. W., "Drag Prediction at Subsonic and Transonic Speeds Using Euler Methods," *Journal of Aircraft*, Vol. 32, No. 4, 1995, pp. 839–845. doi:10.2514/3.46799

[29] Hunt, D. L., Cummings, R. M., and Giles, M. B., "Wake Integration for Three-Dimensional Flowfield Computations: Applications," *Journal of Aircraft*, Vol. 36, No. 2, 1999, pp. 366–373. doi:10.2514/2.2466

[30] van der Vooren, J., and Destarac, D., "Drag/Thrust Analysis of Jet-Propelled Transonic Transport Aircraft: Definition Of Physical Drag Components," *Aerospace Science and Technology*, Vol. 8, No. 6, 2004, pp. 545–556. doi:10.1016/j.ast.2004.03.004

[31] van Dam, C. P., "Recent Experience with Different Methods of Drag Prediction," *Progress in Aerospace Sciences*, Vol. 35, No. 8, 1999,

pp. 751–798.
doi:10.1016/S0376-0421(99)00009-3

[32] Giles, M. B., and Cummings, R. M., "Wake Integration for Three-Dimensional Flowfield Computations: Theoretical Development," *Journal of Aircraft*, Vol. 36, No. 2, 1999, pp. 357–365.
doi:10.2514/2.2465

[33] Chigier, N. A., and Corsiglia, V. R., "Tip Vortices: Velocity Distributions," NASA TM X-62087, Sept. 1971.

[34] Chow, J. S., Zilliac, G. G., and Bradshaw, P., "Mean and Turbulence Measurements in the Near Field of a Wingtip Vortex," *AIAA Journal*, Vol. 35, No. 10, Oct. 1997, pp. 1561–1567.
doi:10.2514/2.1

[35] Van Dyke, M. (ed.), *Album of Fluid Motion*, 10th ed., The Parabolic Press, Stanford, CA, 1982.

[36] Hicken, J. E., and Zingg, D. W., "An Investigation of Induced Drag Minimization Using a Parallel Newton–Krylov Algorithm," *The 12th AIAA/ISSMO Multidisciplinary Analysis and Optimization Conference*, AIAA Paper 2008-5807, Sept. 2008.

[37] von Kármán, T., and Burgers, J. M., "General Aerodynamic Theory: Perfect Fluids," *Aerodynamic Theory: A General Review of Progress*, Vol. 2, Julius Springer, Berlin, 1935.

[38] Spillman, J., "Wing Tip Sails: Progress to Date and Future Developments," *The Aeronautical Journal*, Vol. 91, No. 110, Dec. 1987, pp. 445–453.

[39] Smith, M. J., Komerath, N., Ames, R., Wong, O., and Pearson, J., "Performance Analysis of a Wing with Multiple Winglets," *The 19th AIAA Applied Aerodynamics Conference*, AIAA Paper 2001-2407, 2001.

E. Livne
Associate Editor